Temperatures since the last glacial maximum in the Maritime Alps from cosmogenic noble gas paleothermometry

Marissa M. Tremblay[1,2,*], David L. Shuster[1,2], Matteo Spagnolo[3], Hans Renssen[4], and Adriano Ribolini[5]

[1]Department of Earth and Planetary Science, University of California, Berkeley, Berkeley, CA, 94720-4767 USA

[2]Berkeley Geochronology Center, Berkeley, CA, 94709, USA

[3]Department of Geography and Environment, School of Geosciences, University of Aberdeen, Aberdeen, AB24 3UF, UK

[4]Department of Natural Sciences and Environmental Health, University College of Southeast Norway, 3800 Bø, Norway

[5]Dipartimento di Scienze della Terra, Universita' di Pisa, 56126 Italy.

[*]Now located at Scottish Universities Environmental Research Centre, Rankine Avenue, East Kilbride, G75 0QF, UK

Correspondence to: Marissa M. Tremblay (marissa.tremblay@glasgow.ac.uk)

Abstract

While an extensive network of proxy records has been used to reconstruct climate parameters throughout much of the European Alps during the Late Quaternary, our knowledge of deglacial climate conditions in the Maritime Alps from proxy records is limited. Here, we utilize a new geochemical technique known as cosmogenic noble gas paleothermometry to constrain temperatures in the Maritime Alps since the Last Glacial Maximum (LGM). We measured cosmogenic ^{3}He abundances in quartz from boulders in a series of nested moraines in the Gesso Valley, Italy. Paired with previous constraints on the exposure duration from cosmogenic ^{10}Be measurements and with ^{3}He diffusion experiments on proton-irradiated quartz fragments from the same boulders, we use the cosmogenic ^{3}He abundances to place constraints on the possible temperatures these boulders experienced during their exposure since the LGM. We calculate effective diffusion temperatures over the last ~22 thousand years that range from 8 to 25 ºC. Effective diffusion temperatures (EDTs) are functionally related to but generally several degrees higher than mean ambient temperatures due to the nonlinear dependence of diffusion on temperature. The EDTS we determine from our ^{3}He observations are broadly consistent with temperatures inferred from other proxies in nearby Alpine regions and with temperature estimates from a general circulation model (GCM). In detail, however, we calculate significantly different EDTs for boulders sampled from the same moraines. These discrepancies could result from (1) the fact that we have not accounted for variations in radiative heating of the boulder surfaces (e.g, due to variations in overhead vegetation cover or snow cover), (2) limitations in our understanding of and ability to model accurately complex helium diffusion kinetics, (3) uncertainties associated with our grain size analyses, or (4) some combination of the three. Additional work to understand the effects of radiative heating and to better understand complex

diffusion kinetics is necessary to provide better resolution on temperatures since the LGM in this setting.

1. Introduction

Data from paleoclimate proxies constrain the dynamics of Earth's climate system on timescales inaccessible with the instrumental record. Proxy observations from key intervals of Earth's climatic past, such as the Last Glacial Maximum (LGM) and subsequent deglaciation, allow us to understand how the climate system responds to a change in forcing (e.g., Annan and Hargreaves, 2013; Schmittner et al., 2011; von der Heydt et al., 2016) and evaluate the ability of climate models to simulate the climate system's response (e.g., Annan and Hargreaves, 2015; Harrison et al., 2015; Schmidt et al., 2014) both of which improve our ability to forecast future climate change (e.g., Masson-Delmotte et al., 2013). Terrestrial proxies are particularly important for assessing how changes in large scale ocean-atmosphere dynamics manifest at a regional scale in the continental settings that people inhabit and depend upon.

An extensive network of terrestrial climate reconstructions from fossil pollen and chironomid (midges) records exists across the European Alps since the Last Glacial Maximum (LGM; e.g. Bartlein et al., 2011; Heiri et al., 2014). Despite such an extensive proxy network, our knowledge of deglacial climate conditions in the southern sector of the French and Italian Alps (hereafter referred to as the Maritime Alps) from proxy records is limited. While there are a handful of pollen-based reconstructions from the Maritime Alps of climate parameters through the Holocene, such as mean temperature during the coldest month and mean annual precipitation (Bartlein et al., 2011; Cheddadi et al., 1996; Cheddadi and Bar-Hen, 2009; Davis et al., 2003;

Wu et al., 2007), no reconstruction from the region extend back to the LGM. Similarly, there is only one reconstruction of mean July temperatures from fossil assemblages of chironomids proximal to the Maritime Alps from Lago Piccolo di Avigliana with temporal coverage limited to 14–9.5 thousand years ago (Larocque and Finsinger, 2008). There are two proxy studies from the Maritime Alps that extend into the latest Pleistocene which we are aware of—one reporting pollen fossil assemblages in sixteen high elevation (> 1700 m) lakes (Brisset et al., 2015) and one reporting fossil chironomid assemblages from Lac Long Inférieur in France (Gandouin and Franquet, 2002)—and neither study interprets the proxies in terms of quantitative climate parameters.

Due to the Maritime Alps' (1) southerly latitude, (2) generally lower elevations and (3) proximity to the Mediterranean Sea, the Late Quaternary climatic evolution and glacier dynamics in this region may have differed substantially from those in Alpine regions further north and further inland (e.g., Kuhlemann et al., 2008), despite the apparent synchronicity of glacier advances during the LGM and later stadials recorded by moraines across the Alps (Federici et al., 2017; e.g. Ivy-Ochs et al., 2007; Kuhlemann et al., 2008). Reconstructing temperatures in the Maritime Alps since the LGM would therefore fill a gap in an otherwise extensive network of proxy-based reconstructions of post-LGM climate across the Alps, and address the specific question of how climate evolution in the Maritime Alps during deglaciation may have differed from other Alpine sectors. For example, in combination with the positions and chronology of moraines, a well-resolved local temperature record could be used to inform a simple glacier mass balance model for valleys in the Maritime Alps during the deglacial period. With independent constraints on deglacial temperatures, such a mass balance model could be used to crudely invert for changes in

93 precipitation during deglaciation (e.g. Kessler et al., 2006). This paired temperature-precipitation
94 reconstruction could then be compared to proxy records further north and inland in the Alps to
95 assess how climate and glacier dynamics varied across the region during deglaciation.
96
97 In addition to assessing climatic variability during deglaciation across the European Alps,
98 temperature records from an independent proxy could provide needed tests of different
99 methodologies for reconstructing climate parameters over this time interval. Reconstructions of
100 climate parameters from existing proxies in the European Alps commonly exhibit significant
101 disagreement with climate model simulations prior to the Holocene. Pollen-based reconstructions
102 suggest much colder temperatures, particularly in the winter, than the models predict (e.g. Jost et
103 al., 2005), while models predict higher summertime temperatures than chironomid-based
104 reconstructions during interstadials (Heiri et al., 2014). It is unclear whether these disagreements
105 are attributable to limitations in the global climate models used to simulate paleoclimate, a
106 breakdown in the assumptions of biologically-based reconstructions, or some combination of
107 both. Having independent pre-Holocene temperature records in the European Alps that are
108 mechanistically governed by different processes would therefore help in assessing the cause of
109 the current proxy-model discrepancies.
110
111 Cosmogenic noble gas paleothermometry is a new geochemical technique for reconstructing past
112 Earth surface temperatures (Tremblay et al., 2014a). Cosmogenic nuclides are produced by
113 nuclear interactions between target atoms and high-energy cosmic-ray particles, both in Earth's
114 atmosphere and in the solid Earth. Because the flux of secondary cosmic-ray particles decreases
115 exponentially with depth in rock, production of cosmogenic nuclides is restricted to the

uppermost few meters of the Earth's crust. The near surface production of rare nuclides such as ^{10}Be and ^{26}Al by cosmic-ray particle interactions in common rock-forming minerals like quartz has been extensively developed and utilized by the geomorphology community to date the surface exposure of rocks and quantify erosion rates over the last 25 years (e.g., Granger et al., 2013). Rare noble gas nuclides such as ^{3}He and ^{21}Ne are also produced in minerals by cosmic-ray particle interactions. In common minerals like quartz and feldspars, these noble gases sometimes exhibit diffusive loss at Earth surface temperatures (Gourbet et al., 2012; Shuster and Farley, 2005; Tremblay et al., 2017, 2014b) and thus have not been widely utilized in cosmogenic nuclide studies. However, cosmogenic noble gas–mineral pairs exhibiting open-system behavior (simultaneous production and diffusion) can be utilized to reconstruct the temperatures that rocks experience while exposed to cosmic-ray particles at Earth's surface when paired with observations of a quantitatively retained cosmogenic nuclide. In high latitude and/or high altitude environments, theoretical calculations indicate that measurements of ^{3}He in quartz can record temperature variations from the last glacial period to the present (Tremblay et al., 2014a).

Here, we constrain temperatures since the last glacial maximum (LGM) using observations of cosmogenic ^{3}He abundances in quartz from moraine boulders in the Gesso Valley. The Gesso Valley is located in the southernmost Maritime Alps of Italy approximately 40 km from the Gulf of Genoa in the Mediterranean Sea (Fig. 1) and was glaciated during the last glacial period. Glacial moraines and other geomorphic features have been mapped throughout the basin (Federici et al., 2003), and cosmogenic ^{10}Be exposure ages have been determined for boulders from three moraines that span from the LGM to the Younger Dryas cold period (YD) (Federici et

al., 2017, 2012, 2008). A number of younger, Holocene-age moraines are preserved at higher elevations in the Gesso Valley (Fig. 1), and small glaciers restricted to the highest elevation cirques persist today (Federici et al., 2017). We measured cosmogenic ^{3}He abundances in quartz from a subset of the boulders with ^{10}Be exposure ages from the three previously-studied moraines. We also conducted stepwise degassing experiments to quantify the kinetics of ^{3}He diffusion in quartz from these boulders. Because cosmogenic ^{3}He is simultaneously produced and diffusively lost during exposure in the moraines, the 'apparent' exposure ages we calculate from the measured ^{3}He abundances are younger than the 'true' exposure age determined from the ^{10}Be measurements. The difference between the 'apparent' and 'true' exposure ages can be used to calculate the integrated effective diffusion temperature (EDT) during exposure. This integrated EDT is the temperature corresponding to the mean diffusivity over a variable temperature history, and is therefore a direct function of the ambient temperature history (Tremblay et al., 2014a). Paired with sample-specific ^{3}He diffusion kinetics, we use the difference between 'apparent' and 'true' exposure ages to model the permissible integrated EDTs, and by relation ambient temperature histories, of each boulder. The presence of numerous moraines with different exposure ages within the same valley is advantageous because it allows us to reconstruct temperatures over different time intervals for an area with a shared climate history.

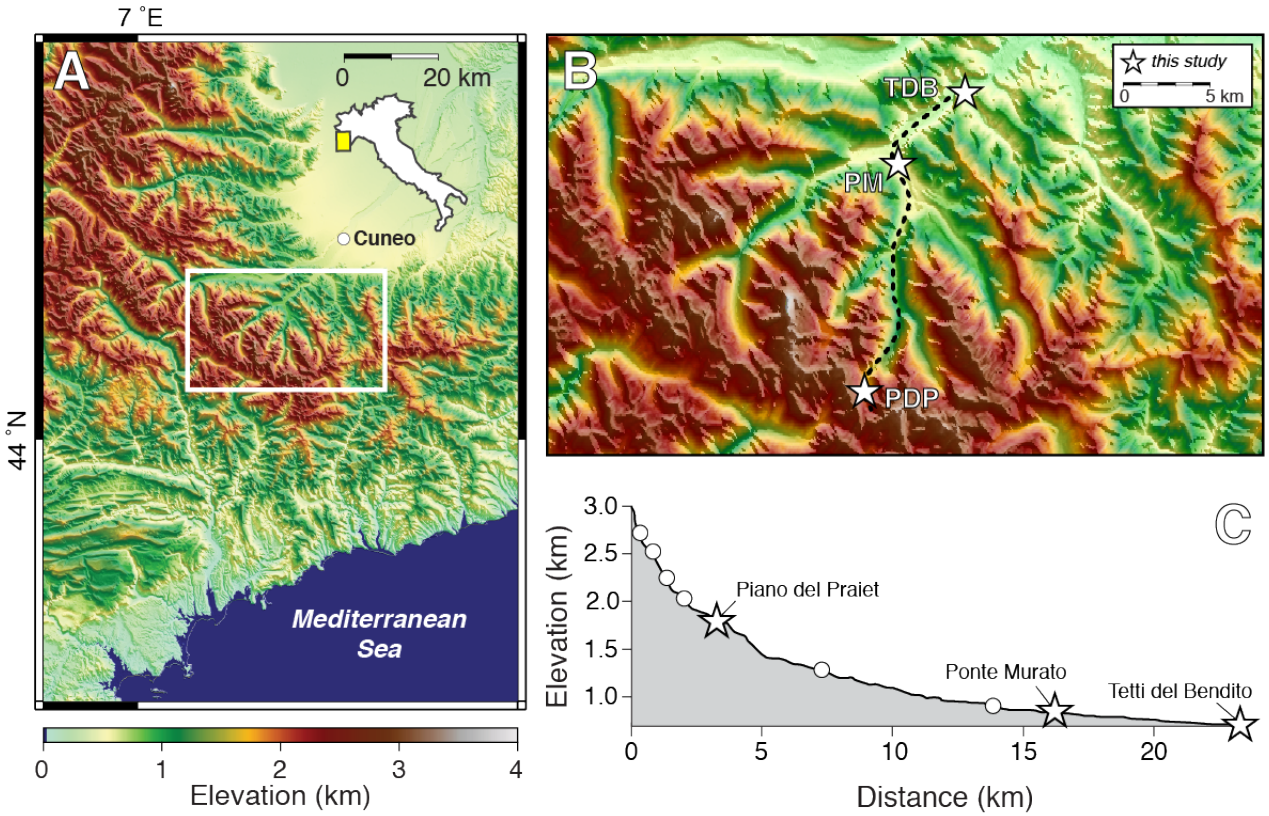

Figure 1: A: Topographic map of the Maritime Alps. Map location is shown in the inset of Italy. White box corresponds to the enlarged view in (B). B: Topography of the Gesso Valley. White stars mark the locations of moraines sampled for this study: Piano del Praiet (PDP), Ponte Murato (PM), and Tetti del Bandito (TDB). Dashed line corresponds to the longitudinal profile shown in (C). C: Longitudinal profile of the Gesso Valley. White stars mark the locations of moraines studied here, as in (B); white circles denote additional moraines in the Gesso Valley not studied here. A detailed map of the geomorphic features in the Gesso Valley is available in Federici et al. (2003).

1.1 Existing proxy constraints on the Late Quaternary climate of the Maritime Alps

Over the historical period, the Maritime Alps have been characterized by warmer mean annual temperatures (MAT), smaller annual temperature amplitudes, lower mean annual precipitation (MAP), and snow cover that is thinner and lasts for smaller fraction of the year than in other Alpine sectors (Durand et al., 2009a, 2009b). The Maritime Alps most likely remained the warmest Alpine sector during the Late Quaternary, given that the Maritime Alps are ~6º south of

the northernmost eastern Alps, and thus would have experienced greater insolation and generally higher temperatures during this time period. Warmer overall conditions is consistent with species distribution and phylogeographical models, which suggest that the Maritime Alps remained warmer than other parts of the Alps and functioned as a refugium for plant species during the last glacial period (Casazza et al., 2016). However, temperature and precipitation anomalies in the Maritime Alps during specific climatic intervals of the Late Quaternary may have been distinct from other Alpine sectors. For example, during the Mid-Holocene Warm period 6,000 years ago, pollen-based reconstructions indicate that Maritime Alps winters may have been as much as 2–3 ºC colder than today, while throughout the rest of the Alps winter temperatures were comparable to today (Bartlein et al., 2011; Cheddadi et al., 1996; Wu et al., 2007). For the same time period, pollen-based reconstructions indicate that the Maritime Alps were wetter ($\Delta P - E > 0$), while the rest of the Alps were drier ($\Delta P - E < 0$) (Bartlein et al., 2011; Cheddadi et al., 1996).

As previously mentioned, no proxy-based reconstructions from the Maritime Alps extend back to the LGM. The nearest pollen-based reconstructions indicate 15–20 ºC colder winter temperatures and ~500 mm/yr lower MAP during the LGM than today (Bartlein et al., 2011; Jost et al., 2005). For the Mediterranean region as a whole, LGM winter temperatures range anywhere from 0 to 30 ºC colder than today, while MAP varies between 0 and 800 mm/yr less than today (Wu et al., 2007). In contrast to pollen-based reconstructions, Kuhlemann et al. (2008) suggested that incursions of cold polar air between the Pyrenees and the Alps were more frequent during the LGM in order to explain spatial patterns of Mediterranean sea surface temperatures (SSTs) and equilibrium line altitude (ELA) depressions. Such cold air incursions would have resulted in greater moist air convection and cyclogenesis as these air masses encountered the warm SSTs in

the Gulf of Genoa and therefore greater precipitation in the Maritime Alps and other Mediterranean-proximal glaciated areas (e.g., Corsica). Although this interpretation of Kuhlemann et al. (2008) is complicated by the fact that the ELA dataset they used is diachronous (Hughes and Woodward, 2017), it nonetheless implies wetter conditions in the Maritime Alps, not dryer as suggested by pollen-based reconstructions, during the LGM and potentially during subsequent stadials marked by glacier re-advances, assuming the same atmospheric phenomena took place.

2. Methods

Of the Gesso Valley boulders for which ^{10}Be measurements exist, we obtained archived material (either whole rock or crushed, sieved fractions) from five samples for cosmogenic ^{3}He measurements: one from the Piano del Praiet (PDP10) moraine, two from the Ponte Murato moraine (PM1, and PM4), and two from the Tetti del Bandito moraine (TDB1 and TDB3; Fig. 1 and Table 1). The ^{10}Be concentration in quartz for PDP10 ($223.8 \pm 9.6 \times 10^3$ atoms/g) was measured at the Scottish Universities Environmental Research Centre Cosmogenic Isotope Analysis Facility in 2013; all other ^{10}Be concentrations are previously published (Federici et al., 2012, 2008). The ^{10}Be exposure ages of these boulders and other boulders from the same moraines have been used to associate the Piano del Praiet, Ponte Murato, and Tetti del Bandito moraines with the Younger Dryas, Buhl, and LGM stadials respectively (Federici et al., 2012, 2008). We obtained a seventh sample, PDP-11, for which there are no existing ^{10}Be measurements. However, probative measurements of neon isotope abundances in PDP-10 and PDP-11 indicated that PDP-11 has a substantial inherited cosmogenic nuclide inventory (i.e., prolonged exposure to cosmic rays before being deposited in the Piano del Praiet moraine) and

212 will therefore not be discussed further. We separated quartz from other phases using standard
213 crushing, sieving, and magnetic methods, followed by a 'frothing' technique commonly used in
214 the ceramics industry to separate quartz from feldspars in the largest sieve fraction that lacked
215 composite grains (Buckenham and Rogers, 1954). Purified quartz was then used to both measure
216 cosmogenic ^{3}He abundances and determine sample-specific ^{3}He diffusion kinetics. All helium
217 isotope measurements were made with an MAP 215-50 sector field mass spectrometer in the
218 BGC Noble Gas Thermochronometry Lab. Gas purification techniques and mass spectrometer
219 analyses are as described in Tremblay et al. (2014b).
220

Sample	Latitude (decimal degrees)	Longitude (decimal degrees)	Elevation (m)	Sample thickness (cm)	Shielding factor
PDP10	44.421534	7.819950	1806	3	0.9200
PM1	44.252667	7.385500	860	3	0.9653
PM4	44.252667	7.385500	860	3	0.9653
TDB1	44.289712	7.432528	770	3	0.9825
TDB3	44.289712	7.432528	770	3	0.9819

Table 1: Locations and sample information for moraine boulders previously dated in the Gesso Valley with cosmogenic ^{10}Be, originally reported in Federici et al. (2012, 2008).

221

222 For cosmogenic ^{3}He measurements, 100–500 mg aliquots of quartz were weighed and packed
223 into tantalum metal cups with both ends crimped, placed under vacuum in a sample chamber,
224 and heated with a feedback-controlled 150 W diode laser to either 500, 800, or 1100 ºC for 15
225 minutes until subsequent extractions yielded He signals indistinguishable from the instrumental
226 detection limit. Empty tantalum cup blanks, heated to the same temperatures as the samples, and
227 room temperature procedural blanks were measured throughout each analytical session and
228 subtracted from the sample measurements; ^{3}He blank corrections were typically 2–3 x 10^{4} atoms.

Aliquots of air and ^{3}He-spiked helium standards of different manometrically-calibrated pipette volumes were analyzed throughout an instrumental tuning period and used to determine helium sensitivities; sensitivities varied linearly over the pressure range of the sample analyses, estimated by the size of the ^{4}He signal. We propagated uncertainties from the blank corrections and sensitivity regression into the cosmogenic ^{3}He concentrations. We assume that all ^{3}He is cosmogenic.

To determine sample-specific diffusion kinetics, we conducted stepwise degassing experiments on a proton-irradiated quartz grain from each sample. Proton irradiation generates a uniform distribution of ^{3}He in quartz through similar nuclear reactions to those induced by cosmic ray particles but with ten orders of magnitude or higher production rates, enabling step degassing diffusion experiments to be conducted on single irradiated quartz grains (Shuster et al., 2004; Shuster and Farley, 2005; Tremblay et al., 2014b). Quartz aliquots were irradiated with a 228.5 MeV proton beam for 6 hours at the Francis H. Burr Proton Therapy Center at the Massachusetts General Hospital in December 2015; the total proton fluence for this irradiation was 9.14×10^{15} p/cm^2. The irradiation target design and setup are detailed in Tremblay et al. (2017). Proton irradiated quartz aliquots were examined with a binocular microscope, and single crystals lacking visible penetrative fractures and inclusions (fluid or mineral) were selected for stepwise degassing. The dimensions of the chosen grains were measured to estimate the spherical equivalent radius used in later calculations to scale the diffusion lengthscale. Details of the stepwise degassing setup and helium measurements are detailed in Tremblay et al. (2014b).

In addition to determining the spherical equivalent radius of the quartz grains used in diffusion

252 experiments, we also determined the spherical equivalent radii of the quartz grains used for
253 cosmogenic measurements and assessed whether these radii are representative of the quartz size
254 distribution in whole rock. Such an assessment is important because if we significantly reduced
255 the grain size of quartz during the crushing process, this could lead to both an underestimation of
256 the diffusion lengthscale to which the diffusion experiment size is scaled and missing
257 cosmogenic ^{3}He from our measurements. First, we photographed and measured the dimensions
258 of at least 100 quartz grains from the sieve fraction of each sample used for comsogenic ^{3}He
259 measurements. We determined major, intermediate, and minor axes of best fitting ellipsoids
260 using the software ImageJ (Abràmoff et al., 2004) and calculated the radius of a sphere with the
261 same surface area to volume ratio for each grain. We compared the spherical equivalent radii
262 calculated using this approach to spherical equivalent radii determined from micro x-ray
263 computed tomography (CT) analyses on a smaller number of grains from the same samples,
264 wherein the grains were mapped in three dimensions with a resolution better than 5 micrometers.
265 CT scans were obtained on the Xradia MicroXCT scanner at the University of Texas at Austin
266 High-Resolution X-ray CT Facility and processed using the software Blob3D (Ketcham, 2005)
267 as described in Tremblay et al. (2017). This comparison demonstrates that the ellipsoid approach
268 consistently overestimates the spherical equivalent radius by ~50%, likely because the ellipsoid
269 method significantly underestimates the surface area of grains. We therefore scaled the spherical
270 equivalent radii from loose grain measurements by a factor 1.5; the distribution of grain sizes
271 from these measurements are shown in Fig. 2. Also shown in Fig. 2 is the probability distribution
272 of spherical equivalent radii of quartz grains in whole rock. To determine this distribution, we
273 determined circular equivalent radii from measured sectional areas of at least 100 quartz grains
274 in thin sections, and inverted the distribution of circular equivalent radii to a distribution of

spherical equivalent radii using the code STRIPSTAR and the methodology described by Heilbronner and Barrett (2013). For PDP10, the thin section was made from the same sample as the sample crushed for cosmogenic ^{3}He measurements. For the PM and TDB moraines, no whole rock material from the original samples was preserved; we therefore collected additional material from boulders exposed atop each of these moraines for thin sections, and assume that the grain size observed in these samples is representative of the samples for which we have cosmogenic ^{3}He data.

For all samples, the distribution of spherical equivalent radii for the sieve fraction has a smaller standard deviation than the radii determined from thin section measurements (Fig. 2), which is not surprising given that the sieving process removes larger and smaller grains. With the exception of the PM samples, we find that the mean spherical equivalent radius of quartz in the sieve fraction is equal to or slightly greater than the mean radius determined from thin section measurements (Fig. 2). The mean quartz radius in the sieve fraction from the PM samples is only slightly smaller than the mean radius from thin section measurements, and the two distributions show significant overlap. Given the good agreement between mean spherical equivalent radii for the sieve fraction and thin section quartz, we assume that the grain size has not been substantially reduced by sample crushing and use the mean and standard deviation of the sieve fraction radii distributions as the appropriate diffusion lengthscale for modeling the diffusion of cosmogenic ^{3}He in each sample.

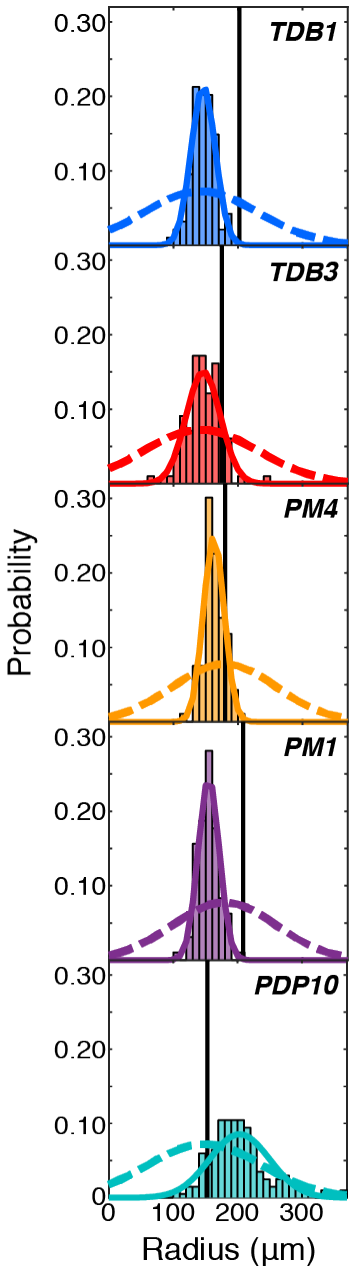

Figure 2: Grain size analysis for Gesso Valley samples. Histograms and solid curves denote the distribution of spherical equivalent radii for representative quartz grains (≥100) from the sieve fraction analyzed for cosmogenic ^{3}He abundances. Dashed curves denote the distribution of spherical equivalent radii in whole rock, inverted from the distribution of sectional circles of quartz grains (≥100) measured in thin section. Thin sections were made from the same sample as the crushed fraction, in the case of PDP10, or from a resampled boulder on the same moraine, in all other cases. Vertical black lines denote the spherical equivalent radius of the single quartz grain analyzed in each diffusion experiment shown in Fig. 4.

296

297 **3. Results**

298 We report measured abundances of cosmogenic ^{3}He in quartz aliquots from each of the Gesso
299 Valley samples in Table 2. We used version 3 (v3) of the online exposure age calculator code, a
300 more recent version of the code published in Balco et al. (2008) that implements the cosmogenic
301 ^{3}He production rate in quartz determined by Vermeesch et al. (2009), to calculate an apparent
302 exposure age from the measured ^{3}He abundance in each aliquot. We assume that the erosion rate
303 is negligible for all boulders sampled, as was assumed in the original publications reporting ^{10}Be
304 exposure ages from these boulders (Federici et al., 2012, 2008). Sample coordinates, elevations,
305 thicknesses, and shielding correction factors used in exposure age calculations are reported in
306 Table 1. In Table 3, we report the weighted mean apparent ^{3}He exposure age for each sample
307 determined using the scaling scheme of Stone (2000). We also recalculated the ^{10}Be exposure
308 ages, normalizing the ^{10}Be concentrations to the isotope ratio standards of Nishiizumi et al.
309 (2007), using v3 of the online exposure calculator and the global ^{10}Be production rate calibration
310 dataset, and assuming the scaling scheme of Stone (2000) (Table 3). We divided the weighted
311 mean apparent ^{3}He exposure ages by the ^{10}Be exposure ages to calculate ^{3}He retention, which
312 represents the fraction of cosmogenic ^{3}He produced during surface exposure that remains in the
313 quartz analyzed (Tremblay et al., 2014a).

314

Sample - aliquot	**Mass of quartz analyzed (g)**	**[^{3}He] (10^{3} atoms/g)**		
PDP10-1	0.109	2.20	±	0.38
PDP10-2	0.101	2.38	±	0.37
PDP10-3	0.102	3.65	±	0.35
PDP10-4	0.126	2.91	±	0.26
PDP10-5	0.121	2.99	±	0.39
PDP10-6	0.136	2.99	±	0.31

PDP10-7	0.117	3.12	±	0.37
PDP10-8	0.125	2.44	±	0.35
PM1-1	0.101	1.14	±	0.42
PM1-2	0.101	0.89	±	0.6
PM1-3	0.304	1.11	±	0.18
PM1-4	0.266	0.88	±	0.15
PM1-5	0.290	1.05	±	0.15
PM4-1	0.113	1.29	±	0.34
PM4-2	0.309	1.51	±	0.17
PM4-3	0.268	1.63	±	0.19
PM4-4	0.247	1.60	±	0.12
TDB1-1	0.216	0.62	±	0.28
TDB1-2	0.269	0.11	±	0.14
TDB1-3	0.306	0.28	±	0.13
TDB1-4	0.292	0.26	±	0.13
TDB1-5	0.482	0.36	±	0.08
TDB3-1	0.216	1.38	±	0.27
TDB3-2	0.124	1.35	±	0.39
TDB3-3	0.279	1.20	±	0.19
TDB3-4	0.301	1.31	±	0.27
TDB3-5	0.268	1.32	±	0.18

Table 2: Observations of cosmogenic ^{3}He in Gesso Valley quartz samples.

315

316 Fig. 3 shows ^{3}He retention as a function of exposure duration in the five samples we analyzed.
317 All Gesso Valley samples retain less than 50% of the cosmogenic ^{3}He that was produced during
318 their exposure (Table 3, Fig. 3). Retention generally decreases with increasing exposure

duration: quartz from PDP10, sampled from the highest elevation moraine with an exposure age of 14071 ± 1220 years, retains 46% of its cosmogenic ^{3}He, while quartz from TDB1, sampled from the lowest elevation moraine with an exposure age of 23397 ± 2072 years, retains only 6% of its cosmogenic ^{3}He. Samples PM1 and PM4, both from the Ponte Murato moraine, have ^{10}Be exposure ages that agree within uncertainty (16356 ± 1601 years and 19213 ± 1654 years, respectively) but significantly different ^{3}He retention (0.28 ± 0.04 versus 0.36 ± 0.04, respectively; Table 3, Fig. 3). Similarly, the ^{10}Be exposure ages for the two Tetti del Bandito moraine samples, TDB1 and TDB3, are in agreement (23397 ± 2072 years and 21003 ± 1854 years, respectively), but the ^{3}He retentions in these two samples are drastically different (0.06 ± 0.01 versus 0.29 ± 0.04, respectivley; Table 3, Fig. 3).

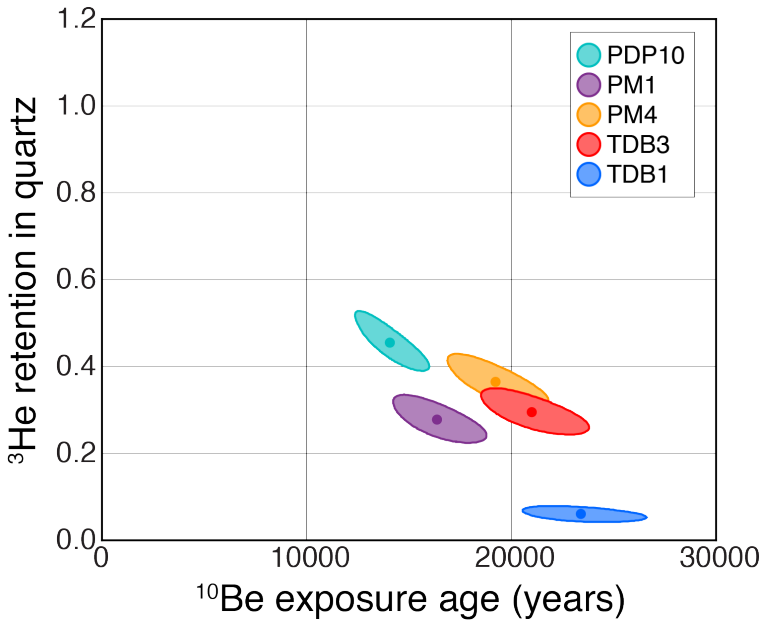

Figure 3: Cosmogenic ^{3}He retention as a function of ^{10}Be exposure age in quartz from Gesso Valley moraine samples. Ellipses represent 1σ uncertainty.

Sample	Apparent exposure age (yr), ^{3}He			Exposure age (yr), ^{10}Be			^{3}He retention		
PDP10	6402	±	341	14071	±	1220	0.46	±	0.05
PM1	4534	±	452	16356	±	1601	0.28	±	0.04
PM4	7006	±	512	19213	±	1654	0.36	±	0.04
TDB1	1407	±	271	23397	±	2072	0.06	±	0.01
TDB3	6187	±	561	21003	±	1854	0.29	±	0.04

Table 3: Apparent ^{3}He exposure ages and retention in Gesso Valley quartz samples. See text for details about the input parameters to the exposure age calculation. We report external uncertainties for both ^{3}He and ^{10}Be exposure ages.

331

332 In order to reconstruct effective diffusion temperatures (EDTs), and by relation temperature
333 histories, from the observed ^{3}He retention in quartz from each sample and assess the differences
334 in ^{3}He retention between samples from the same moraine, we need to know the diffusion kinetics
335 of ^{3}He in each sample. Fig. 4 shows the results of step degassing experiments on proton-
336 irradiated quartz from the Gesso Valley samples in Arrhenius plots where the natural log of
337 diffusivity, calculated from the cumulative fraction of gas released during each heating step
338 (Fechtig and Kalbitzer, 1966), is plotted as a function of inverse temperature (gray circles).

339

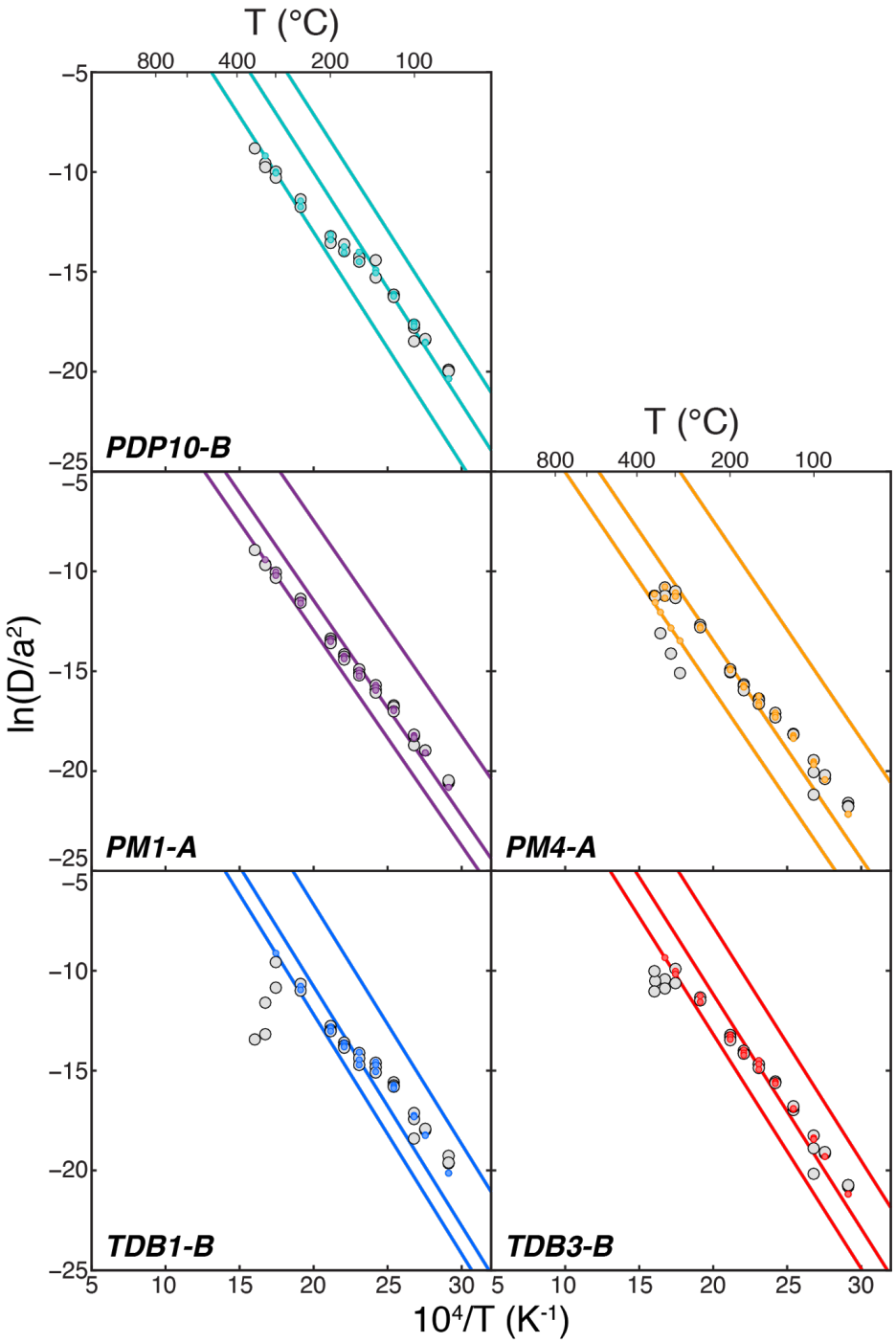

Figure 4: Arrhenius plots for helium diffusion experiments on Gesso Valley quartz samples. D/a^2 values are normalized to s^{-1}. Experimental data are plotted as gray circles. Diffusivities were calculated using the equations of Fechtig and Kalbitzer (1966) and the uncertainty propagation outlined in Tremblay et al. (2014b). Color circles and lines denote three-domain multiple diffusion domain (MDD) models that minimize misfit with the experimental data. Tremblay et al. (2017) describe MDD modeling approach used here.

All Gesso Valley quartz samples exhibit some degree of nonlinearity in the Arrhenius plots (Fig. 4). While we do not have a mechanistic explanation or model for this type of complex diffusion behavior (Tremblay et al., 2014b), multiple diffusion domain (MDD) models (Harrison et al., 1991; Lovera et al., 1991; Lovera and Richter, 1989) can reproduce the nonlinearity observed in laboratory degassing experiments and appear to be relevant to ^{3}He diffusive loss over 10^3–10^4 year timescales, as demonstrated for a geologic case study for which the temperatures during surface exposure are reasonably well known (Tremblay et al., 2014b). We constructed MDD models optimized to fit each of the helium step degassing experiments on Gesso Valley quartz samples following the approach outlined in Tremblay et al. (2017). Fig. 5 shows the misfit between the calculated diffusivities from MDD models and the experimentally-determined diffusivities as a function of number of diffusion domains, where the misfit statistic was calculated as in Tremblay et al. (2017). The misfit shown for a given number of diffusion domains is the minimum misfit found after searching over a large range of model parameters (activation energy E_a, pre-exponential factor(s) D_0/a^2, and gas fraction(s)).

We found that, for all five step degassing experiments, increasing the number of diffusion domains from 1 to 2 and from 2 to 3 significantly reduced the misfit between the observed diffusivities and those calculated with the MDD model (Fig. 5). However, increasing the number of diffusion domains from 3 to 4 did not significantly reduce the misfit between the observed and calculated diffusivities (Fig. 5). For experiment PM1-A, attempts at constructing a four-domain model yielded two domains with the same pre-exponential factor and thus are the equivalent of the three-domain model. Therefore for all experiments we use the diffusion parameters corresponding to the optimized three domain model. Lines corresponding to the diffusion

363 parameters of the three domains, as well as the calculated diffusivities for the three domain
364 models, are shown in color over the experimentally determined diffusivities in Fig. 4. The
365 activation energies, pre-exponential factors, gas fractions, and misfit statistic for these three
366 domain models are reported in Table 4.

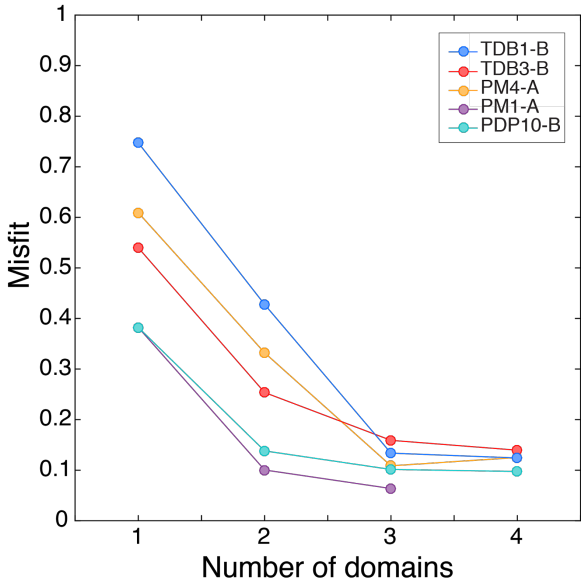

Figure 5: Minimized misfit between observed and MDD-modeled ^{3}He diffusivities as a function of number of diffusion domains for Gesso Valley quartz samples. We increased the number of diffusion domains in our MDD models until the addition of another diffusion domain did not significantly reduce the misfit between the observed and calculated diffusivities. For all Gesso Valley quartz samples, we found that increasing the number of domains from three to four only marginally improved the misfit; therefore we use three-domain MDD models in subsequent calculations. For experiment PM1-A, attempts at constructing a four domain model yielded two domains with the same pre-exponential factor and thus are the equivalent of the three domain model.

367

Experiment	Domain	E_a (kJ/mol)	$\ln(D_0/a^2)$	fraction	Misfit
PDP10-B	1	96.5	10.2	0.61	0.097
	2		16.1	0.21	
	3		13.2	0.18	
PM1-A	1	89.6	8.6	0.54	0.067
	2		10.1	0.36	
	3		14.1	0.1	

PM4-A	1	90.9	8.4	0.74	0.109
	2		5.9	0.2	
	3		14.4	0.06	
TDB1-B	1	99.7	11.8	0.46	0.161
	2		13.2	0.3	
	3		17.3	0.24	
TDB3-B	1	97.6	10.3	0.42	0.149
	2		12.3	0.41	
	3		15.7	0.17	

Table 4: Three domain multiple diffusion domain model parameters for ^{3}He diffusion experiments in Gesso Valley quartz samples.

As discussed in Section 2, we need to scale the diffusion kinetics determined from the step degassing experiments to the diffusion lengthscale appropriate for the cosmogenic ^{3}He abundance measurements. In constructing MDD models, we cannot independently parameterize the diffusivity at infinite temperature, D_0, and the diffusion lengthscale, a. Instead, we model them together as the natural logarithm of the pre-exponential factor in the Arrhenius expression, $ln(D_0/a^2)$, which in an Arrhenius plot corresponds to the y-intercept. Because we cannot independently model the diffusion lengthscale a, we must make an assumption about how to scale the MDD models appropriately. This is not a problem for the ^{40}Ar/^{39}Ar thermochronometry community in which MDD models were developed, because in almost all cases argon diffusion kinetics and naturally-occurring argon isotope abundances are measured in the same mineral grain (e.g. Lovera et al., 1997/8). Here, we assume that the diffusion lengthscale of all domains, and by inference all the pre-exponential factors in a given MDD model, scales with the spherical equivalent radius of the quartz grain analyzed. Theoretically, this implies that diffusion lengthscale of the most retentive domain (the domain with the lowest $ln(D_0/a^2)$ or intercept in Arrhenius space) is the spherical equivalent radius of the grain analyzed. Practically, this scaling

384 is accomplished as follows:

385

386 $$\left(\frac{D_0}{a^2}\right)_{scaled} = \left(\frac{D_0}{a^2}\right)_{MDD} \left(\frac{a_{sde}^2}{a_{cosmo}^2}\right) \quad (1)$$

387

388 where a_{sde} is the spherical equivalent radius of the step degassing experiment quartz grain and
389 a_{cosmo} is the spherical equivalent radius of the quartz grains used for the cosmogenic ^{3}He
390 measurements (Fig. 2).

391

392 With the scaled, sample-specific diffusion kinetics, we explore possible temperature scenarios to
393 explain the observed cosmogenic ^{3}He abundances in the Gesso Valley samples. To do this, we
394 use forward models of simultaneous production and diffusion to model how cosmogenic ^{3}He
395 retention evolves as a function of exposure duration under different temperature scenarios. We
396 begin with the simplest possible scenario of constant temperature over time, as this allows us to
397 assess the EDT integrated over the exposure duration of each sample. These EDTs are equal to
398 or greater than the mean temperatures the samples experienced over their exposure durations
399 because of the nonlinear relationship between diffusivity and temperature (Tremblay et al.,
400 2014a). Fig. 6 shows the evolution of ^{3}He retention as a function of exposure duration for
401 constant temperature scenarios in 2 ºC increments from 0 ºC to 30 ºC. These retention evolution
402 curves differ for each Gesso Valley quartz sample for several reasons: (1) each sample has a
403 different set of diffusion kinetics, assuming a three domain diffusion model (Fig. 4, Table 4), (2)
404 these sample specific diffusion kinetics are scaled to different spherical equivalent radii based on
405 the measured grain size distributions of quartz in the sieve fraction used for cosmogenic ^{3}He
406 measurements (Fig. 2), and (3) the cosmogenic ^{3}He production rate in quartz differs between

407 samples. In each panel of Fig. 6 we report the integrated EDT that agrees with the observed
408 cosmogenic ^{3}He retention in each quartz sample. We provide two uncertainty estimates on this
409 integrated EDT. One σ EDT uncertainties in parentheses account for the uncertainty in ^{3}He
410 retention and an exposure duration as determined from ^{10}Be measurements; the second set of
411 uncertainties also account for uncertainty in the spherical equivalent radius to which the
412 experimentally-determined diffusion kinetics are scaled.
413
414 The most readily observable feature of the models in Fig. 6 is that the integrated EDT calculated
415 for each quartz sample is different. This is in part expected because the different moraines
416 represented by these samples are located at different elevations in the Gesso Valley, and thus will
417 experience different temperatures at any point in time due to the atmospheric lapse rate. This
418 may also in part be due to the samples having different exposure durations; for example, a
419 change in temperature between the deposition of the TDB moraine and the PM moraine would
420 only be reflected in the cosmogenic ^{3}He retention and integrated EDT of the TDB moraine
421 samples. Differences in integrated EDT between samples from the same moraine, on the other
422 hand, are unexpected. For PM1 we calculate an integrated EDT of 7.6 ºC, while for PM4 we
423 calculate a much higher integrated EDT of 19.7 ºC. Similarly, for TDB1 we calculate an
424 integrated EDT of 24.5 ºC, while for TDB3 we calculate a much lower integrated EDT of 15.8
425 ºC.
426

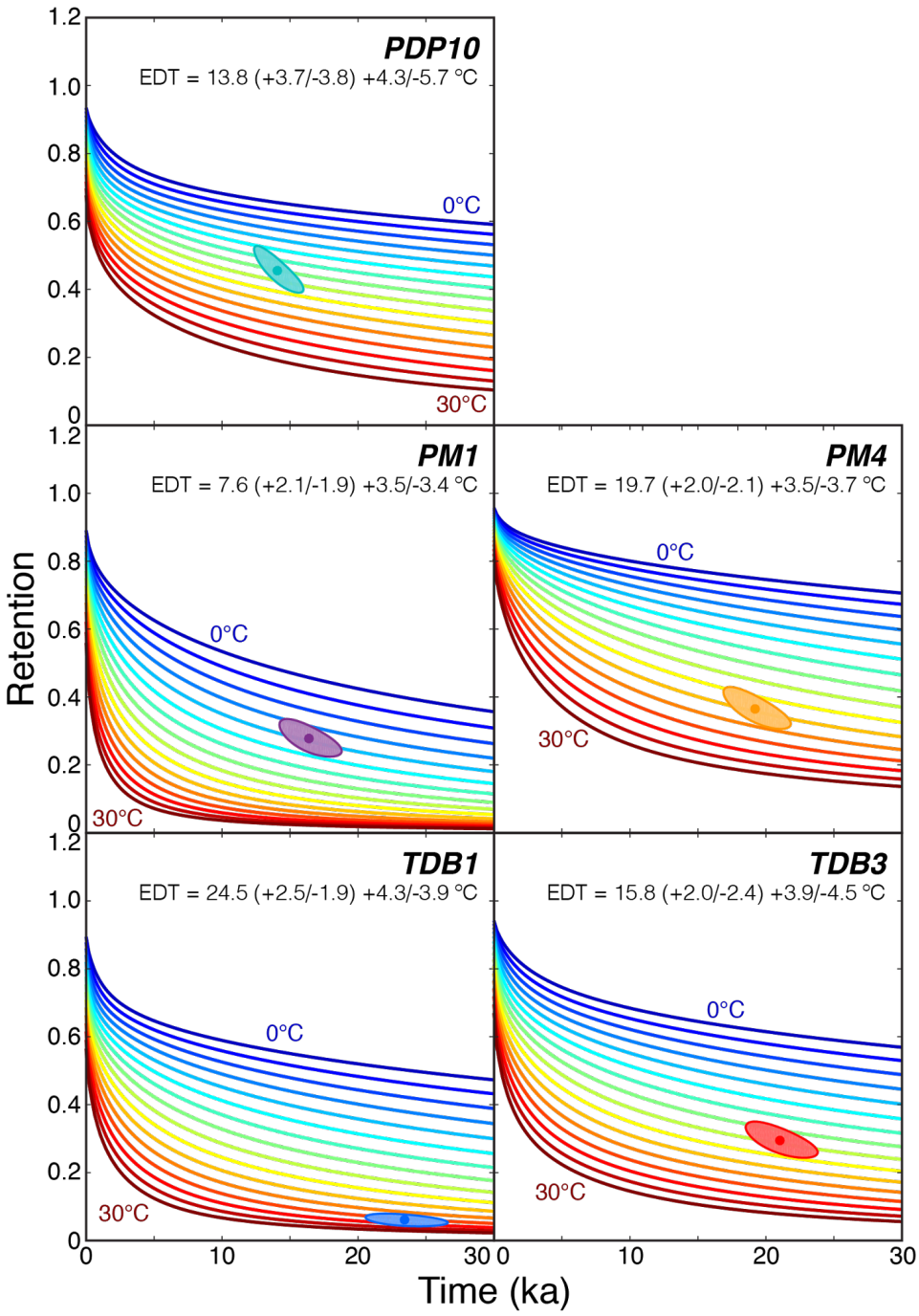

Figure 6: EDTs integrated over the exposure duration of Gesso Valley moraine samples. For each sample, we plot cosmogenic ^{3}He retention as a function of exposure duration assuming a constant EDT and the MDD model diffusion kinetics reported in Table 3. Observed cosmogenic ^{3}He retention ellipses are plotted as in Fig. 4 for comparison. One σ EDT uncertainties in parentheses account for the uncertainty in ^{3}He retention and exposure duration as determined from ^{10}Be measurements; the second set of uncertainties also account for uncertainty in the spherical equivalent radius to which the experimentally-determined diffusion kinetics are scaled.

To put these integrated EDTs into context, in Fig. 7 we use modern daily temperature records from 2002 to 2016 to calculate mean temperatures (solid lines) and EDTs (dashed lines) at the elevation of each moraine. We obtained temperature records at the elevation of each moraine by scaling daily mean, minimum, and maximum temperature data from two meteorological stations within the Gesso Valley: Diga della Piastra (44.227 ºE, 7.389 ºN, 959 m) and Diga del Chiotas (44.168 ºE, 7.334 ºN, 1980 m). These data are publicly available through the Environmental Protection Agency for the Piemonte Region (arpa.piemonte.gov.it). We scaled the temperature data at Diga della Piastra to the elevation of the TDB and PM moraines and the temperature data at Diga del Chiotas to the elevation of the PDP moraine using monthly average lapse rates determined from the same dataset, and calculated the modern EDT using these scaled temperature data and the activation energies of the best fit MDD models in Fig. 4 and Table 4. For PDP10, PM4, and TDB1, the modern EDT estimate (9.8, 15.1, and 15.9 ºC) is several degrees lower than the EDT integrated over each sample's exposure duration (13.8, 19.7, and 24.5 ºC). In contrast, the modern EDT estimate for TDB3 (15.9 ºC) is comparable to the EDT integrated over its exposure duration (15.8 ºC), and for PM1 the modern EDT estimate (15.0 ºC) is several degrees higher (vs. 7.6 ºC).

In addition to comparing the integrated EDTs calculated from observed cosmogenic ^{3}He abundances to modern day EDTs in the Gesso Valley, we can compare our cosmogenic ^{3}He observations to the those that would be result (1) from temperature histories simulated in general circulation models (GCMs), and (2) from temperature reconstructions based on other proxies at nearby locations. For both model and proxy comparisons, the temperature history used to model cosmogenic ^{3}He abundances must be equal in duration to the moraine sample exposure.

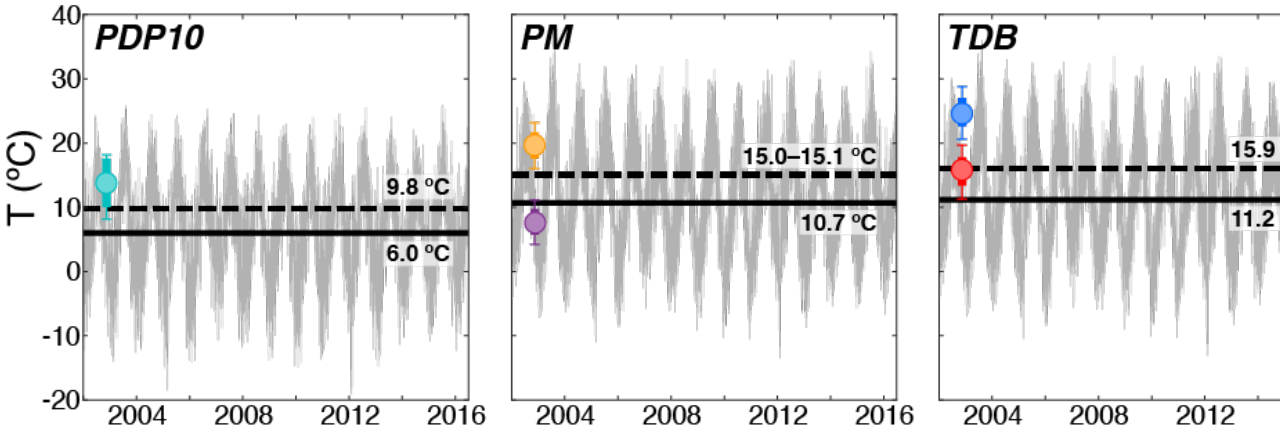

Figure 7: EDTs calculated from modern meteorological data. In gray we show the time series of mean, minimum, and maximum daily temperatures from 2002 to mid-2016 at the elevations of the PDP, PM, and TDB moraines, scaled from the nearest two meteorological stations using average monthly lapse rates. Solid black bars denote the mean temperature for each time series; dashed black bars denote the modern EDT for each time series calculated using the activation energies of the best fit MDD models in Fig. 4 and Table 4. EDTs integrated over the exposure duration of each sample are also shown for comparison as circles, with colors for specific samples and 1σ uncertainties as reported in Fig. 6.

Most GCM paleo-experiments simulate climate at a particular point in time, such as the mid-Holocene or LGM; only a handful of GCMs simulations have explored transient climate evolution in the Holocene and latest Pleistocene. Here, we model how cosmogenic ^{3}He retention would evolve as a function of exposure duration using seasonal temperature outputs from the TraCE-21ka transient simulation. TraCE-21ka uses the National Center for Atmospheric Research (NCAR) Community Climate System Model version 3 (CCSM3), a synchronously coupled atmosphere-ocean general circulation model (GCM) (Collins et al., 2006), to simulate the Earth's climate from the LGM (22 thousand years ago) to the present (He, 2011; Liu et al., 2009). We obtained seasonal (DJF, MAM, JJA, and SON) mean and maximum temperatures from the TraCE-21ka simulation for the 44.3 ºN, 7.4 ºE grid cell including the Gesso Valley. These simulated temperatures were determined for a mean elevation above sea level for the grid

462 cell, which changed through the simulation as simulated sea level changed. However, the
463 elevation of our sample sites with respect to sea level would have also changed through time,
464 meaning that the relative offset between our sample site elevation and the mean grid cell
465 elevation would have remained constant. We therefore scale the TraCE-21ka simulation
466 temperatures to our sample sites using the present day difference between the sample site
467 elevations and TraCE-21ka mean elevation assuming the modern seasonal lapse rate determined
468 from the meteorological stations discussed above. The atmospheric lapse rate in the Gesso
469 Valley likely changed between the LGM and the present, especially considering the fact that the
470 valley was more extensively glaciated during part of this interval. Nonetheless, we assume the
471 modern rate because (1) we have no independent means for assessing how different paleo-lapse
472 rates may have been, and (2) any differences from the modern lapse rate when the valley was
473 glaciated were likely ≤ 2 ºC/km (e.g. Davis et al., 2003; Gardner et al., 2009; Loomis et al.,
474 2017), which will not be resolvable using our cosmogenic noble gas observations that span ≤ 1
475 km in elevation (Tremblay et al., 2014a).
476
477 For all Gesso Valley quartz samples, the observed cosmogenic ^{3}He retention is bracketed by the
478 ^{3}He retention calculated assuming mean seasonal temperatures and the ^{3}He retention calculated
479 assuming maximum seasonal temperatures scaled from the TraCE-21ka simulation. For PDP10
480 (Fig. 8), PM4 (Fig. 9), and TDB1 (Fig. 10), we calculate cosmogenic ^{3}He retention from the
481 TraCE-21ka simulation maximum seasonal temperature that is in agreement within uncertainty
482 with the observed retention in these samples. Cosmogenic ^{3}He retention calculated from the
483 TraCE-21ka mean seasonal temperatures agrees with the observed cosmogenic ^{3}He retention in
484 PM1 within uncertainty (Fig. 9), while for TDB3 the observed cosmogenic ^{3}He retention lies

485 between that predicted from the mean and maximum seasonal TRACE-21ka temperatures.

486

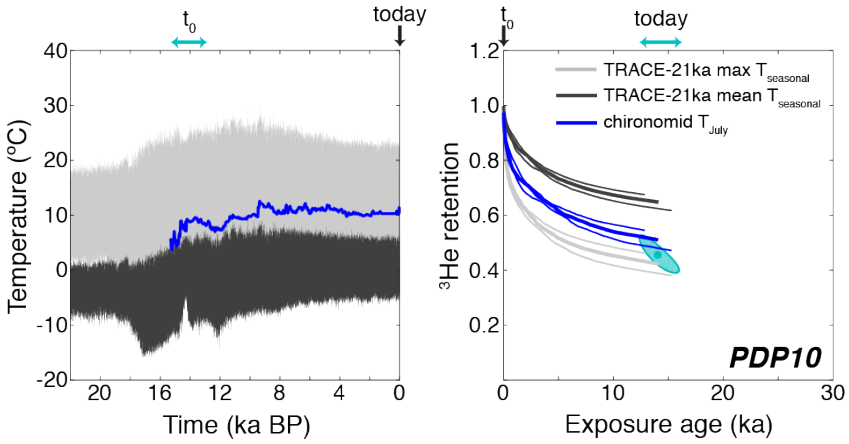

Figure 8: Cosmogenic ^{3}He retention in PDP10 quartz calculated from scaled TraCE-21ka seasonal temperatures and scaled, spliced chironomid July temperatures. The left panel shows the mean (black) and maximum (gray) seasonal temperature from the TraCE-21ka climate simulation and the mean July temperature (blue) from four spliced chironomid records, scaled to the elevation of PDP10 using modern lapse rate data and, for the chironomid records, weighted by distance from our study site. The right panel shows the evolution of ^{3}He retention with time assuming the TraCE-21ka and chironomid temperatures represent the EDT experience over PDP10's exposure duration. Thick retention curves assume the mean exposure duration and grain size for diffusion kinetics scaling; lower thin retention curves assume the +1σ exposure duration and grain size, while upper thin curves assume the –1σ exposure duration and grain size. The ellipse shows the observed retention and exposure duration, as in Fig. 3.

487

488

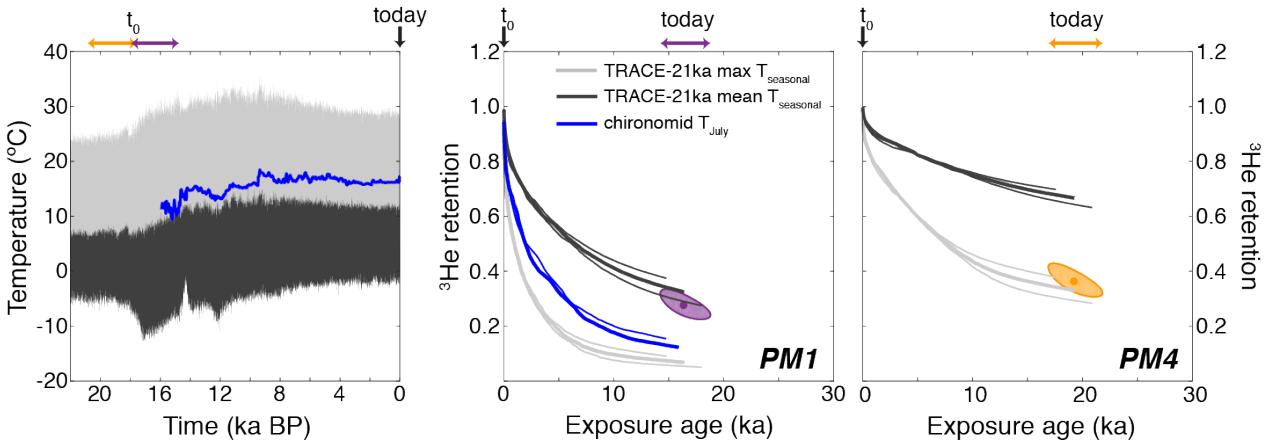

Figure 9: Cosmogenic ^{3}He retention in PM1 and PM4 calculated from scaled TraCE-21ka seasonal temperatures and, in the case of PM1, scaled, spliced chironomid July temperatures. The left panel shows the mean (black) and maximum (gray) seasonal temperature from the TraCE-21ka climate simulation and the mean July temperature (blue) from four spliced chironomid records, scaled to the elevation of PM using modern lapse rate data and, for the chironomid records, weighted by distance from our study site. The right panels show the evolution of ^{3}He retention with time assuming the TraCE-21ka and chironomid temperatures represent the EDT experience over the PM samples' exposure duration. Thick and thin retention curves are as in Fig. 8. Ellipses show the observed retention and exposure duration, as in Fig. 3.

489

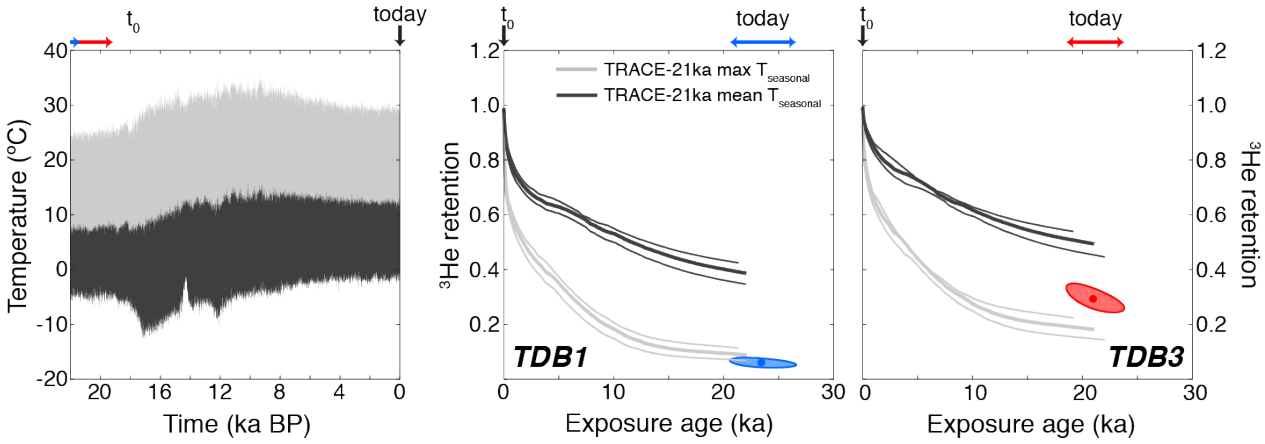

Figure 10: Cosmogenic ^{3}He retention calculated in TDB1 and TDB3 from scaled TraCE-21ka seasonal temperatures. The left panel shows the mean and maximum seasonal temperature from the TraCE-21ka climate simulation, scaled to the elevation of the TDB moraine using modern lapse rate data. The right panels shows the evolution of ^{3}He retention with time assuming the TraCE-21ka temperatures represent the EDT experience over the TDB samples' exposure duration. Thick and thin retention curves are as in Fig. 8. Ellipses show the observed retention and exposure duration, as in Fig. 3.

We also use chironomid-based July temperature reconstructions from other Alpine locations to model cosmogenic ^{3}He retention for comparison with our cosmogenic ^{3}He observations. The lack of Alpine chironomid records before 16 cal. years BP prevents us from using chironomid-based July temperature reconstructions to model cosmogenic ^{3}He retention in PM4, TDB1, and TDB3. However, we can splice together chironomid records from several locations to obtain coeval coverage with samples PDP10 and PM1, which have the youngest ^{10}Be exposure ages of 14071 ± 1220 and 16356 ± 1601 years, respectively. The most proximal chironomid-based mean July temperature reconstruction is from Lago Piccolo di Avigliana (LPA), located in the Italian Alps ~80 km north of the Gesso Valley (45.05 ºN; 7.38 ºE, 365 m), where the record extends from 14200 to 9500 cal. year BP (Larocque and Finsinger, 2008). In order to obtain coeval coverage with the exposure ages of PDP10 and PM1, we spliced the LPA record with chironomid July temperature reconstructions from: Schwarzsee ob Sölden (SOS), a high-alpine lake in the Austrian Alps (46.96583 ºN, 10.94611 ºE, 2796 m) with a chironomid record from 10200 to –36 cal. years BP (Ilyashuk et al., 2011); Lac Lautrey (LAU), a small lake in the French Jura Mountains (46.58722 ºN, 5.86389 ºE, 788 m) with a chironomid record from 15908 to 11033 cal. years BP (Heiri and Millet, 2005); and Hinterburgsee (HIN), a subalpine lake in the northern Swiss Alps (46.71833 ºN, 8.06750 ºE, 1515 m) with a chironomid record from from 12210 to 1900 cal. years BP (Heiri et al., 2004). Like the GCM simulation, we scaled the July temperature reconstructions from each location to the elevations of PDP10 and PM1 using modern lapse rate information, and when temporal overlap occurred between two or more chironomid records we used an average of the scaled temperatures weighted by the inverse distance between the chironomid sites and our study site. In Figs. 8 and 9 we show the scaled,

513 spliced July temperature reconstruction using all four chironomid records and the corresponding
514 model for cosmogenic ^{3}He retention in PDP10 and PM1, respectively. We found that different
515 chironomid record splices (e.g., SOS + LPA; SOS + HIN + LPA; SOS + LPA + LAU; SOS +
516 HIN + LPA +LAU) result in very small differences in modeled cosmogenic ^{3}He retention;
517 therefore only the four record splice (SOS + HIN + LPA +LAU) is shown. Like the maximum
518 seasonal temperatures from the TraCE-21ka simulation, we model cosmogenic ^{3}He retention
519 from the mean July temperature reconstruction that agrees with our observations from PDP10
520 and that underestimates the observed ^{3}He retention in PM1.
521
522 **4. Discussion**
523 To a first order, the fact that modern EDTs calculated from meteorological data are within a few
524 degrees of the EDTs integrated over the exposure duration of each Gesso Valley quartz sample,
525 and the fact that cosmogenic ^{3}He retention calculated with temperatures from a GCM simulation
526 and an independent proxy reconstruction are in broad agreement with our cosmogenic ^{3}He
527 observations, is promising. This first order agreement suggests that our cosmogenic ^{3}He
528 measurements are, in fact, providing information on ambient temperature conditions during
529 exposure. For example, we do not calculate integrated EDTs below 0 ºC, as we do for
530 cosmogenic ^{3}He measurements made on Holocene-age glacial erratics in Antarctica (Tremblay et
531 al., 2014a), nor do we calculate integrated EDTs unfeasibly high for Earth surface conditions
532 (e.g, EDTs of 70–80 ºC that we obtain for the Moon (Shuster and Cassata, 2015). The apparent
533 agreement of some of our cosmogenic ^{3}He observations with maximum seasonal temperatures
534 from the TraCE-21ka simulation, which has a 3.75º resolution, and with July temperatures
535 reconstructed from Alpine chironomid records spread over hundreds of kilometers, also suggests

536 that the integrated temperature history of the Maritime Alps since the LGM may not have been
537 exceptionally different from those in Alpine regions further north and further inland. However,
538 for the purposes of reconstructing past climate variations, the substantial intra-moraine
539 differences in EDTs are problematic and require explanation. For both the PM and TDB
540 moraines, the difference in integrated EDTs between samples from the same moraine is ~10 ºC.
541
542 One possibility is that these intra-moraine temperature differences are real and reflect differential
543 shading of the samples by vegetation, snow cover or topography. For example, patchy vegetation
544 on a moraine crest may cause one boulder to be fully shaded under a tree canopy, while another
545 boulder tens of meters away remains unshaded. Similarly, boulders nearby to one another might
546 accumulate substantial or insignificant snow cover depending on their relative positioning and
547 shielding from prevailing winds during the wintertime. Unshaded rock samples can experience
548 significantly higher daytime temperatures due to insolation than shaded samples. As discussed in
549 Tremblay et al. (2014a), heating of rocks due to incident solar radiation can substantially raise
550 rock temperatures above daily maximum air temperatures. Amplification of temperatures 5–10
551 ºC above the daily maximum is common in non-desert environments (Bartlett et al., 2006; Hall et
552 al., 2005; McGreevy, 1985; Schwarz et al., 2012). Considering our modern EDT calculations
553 from meteorological station data, if we increase the maximum daily temperature by 5 or 10 ºC,
554 we find significant increases in the EDT. For example, using the diffusion kinetics for TDB1, by
555 increasing the maximum daily temperature in the meteorological data by 5 ºC, we find that EDT
556 increases from 15.9 to 19.2 ºC. Increasing the maximum daily temperature by 10 ºC increases the
557 EDT to 23.0 ºC, which is within the uncertainty of the EDT integrated over TDB1's exposure
558 duration. Therefore it is possible that, in the case of the TDB moraine, TDB3 may have been

559 shaded or snow covered during all or some of its exposure history, while TDB1 was fully
560 exposed to incoming solar radiation throughout its exposure. Similarly, PM1 may have been
561 shaded or snow covered while PM4 was not since the PM moraine was deposited.
562
563 This interpretation is consistent with the comparison of observed cosmogenic ^{3}He retention to
564 calculated retention from TraCE-21ka and chironomid temperatures. TraCE-21ka simulation
565 maximum seasonal temperature calculations agree well with PDP10, PM4, and TDB1
566 observations, while observations from PM1 and TDB3 are closer to the calculations with the
567 mean seasonal temperature from TraCE-21ka. We would expect mean temperatures to agree
568 with our cosmogenic ^{3}He observations, as is the case for PM1, if no heating due to insolation
569 occurred. Following the same reasoning, we anticipate that samples experiencing nonzero
570 insolation will have cosmogenic ^{3}He abundances that are lower than what is expected from mean
571 air temperatures, as is the case for PDP10, PM4, TDB1, and TDB3. Likewise, the good
572 agreement between the observed cosmogenic ^{3}He retention in PDP10 and the chironomid-based
573 reconstruction of mean July temperatures, which will be significantly greater than mean
574 temperatures throughout most of the year, supports the interpretation that the temperatures
575 experienced by sample PDP10 exceeded air temperatures during its exposure to cosmic ray
576 particles. Relating maximum seasonal air temperatures or mean July air temperatures to
577 insolation-induced daily rock temperature amplifications is not straightforward, although an
578 empirical relationship could be obtained by monitoring *in situ* rock temperatures adjacent to
579 meteorological stations.
580
581 We note that shading from solar radiation and shielding of cosmic rays are not equivalent.

582 Vegetative cover can have a substantial effect on heating by insolation, but in most cases a
583 negligible effect on cosmogenic nuclide production rates due to its relatively low density.
584 Similarly, thin snow cover will not substantially affect cosmogenic nuclide production rates but
585 will cause rock temperatures to differ substantially from air temperatures. Thick snow cover ($\geq$ 1
586 m) will affect both production rates and temperatures. Today, there is significant vegetation
587 cover on the TDB and PM moraines, but no cover at PDP. Unfortunately, we have no way of
588 assessing the degree of vegetation cover on the TDB and PM moraines before the modern, and
589 no way to assess the past degree of snow cover for all moraines. Topography can shield rocks
590 from cosmic ray particles, but these effects are accounted for in our calculations of cosmogenic
591 nuclide production rates (Table 1); in contrast, we have not accounted for the effects of
592 topographic shading on rock surface temperatures. We do not have detailed enough locations for
593 the TDB and PM samples to identify the original boulders that were sampled and assess
594 differences in topographic shading, although we suspect this would be secondary to vegetation
595 and snow cover effects.
596
597 Another possible explanation for the intra-moraine differences is that our MDD model
598 representations of helium diffusion kinetics in Gesso Valley quartz samples are inaccurate and/or
599 inadequate. The MDD models we construct are inherently non-unique, and while the models we
600 use minimize the misfit between the observed and calculated diffusivities in our step degassing
601 experiments for a given number of domains, comparable fits can be achieved over a range of
602 diffusion parameters. To illustrate this, in Fig. 11 we show minimized values of MDD model
603 misfit, calculated using the misfit statistic defined in Tremblay et al. (2017), as a function of
604 activation energy E_a for three domain models fit to each of the step degassing experiments

shown in Fig. 4. For most of the step degassing experiments, there is a broad range of activation energies (and associated pre-exponential factors and gas release fractions) over which the misfit with the MDD model changes only slightly; these changes in misfit are much smaller than the change in misfit associated with increasing the number of diffusion domains and the model complexity (Fig. 5).

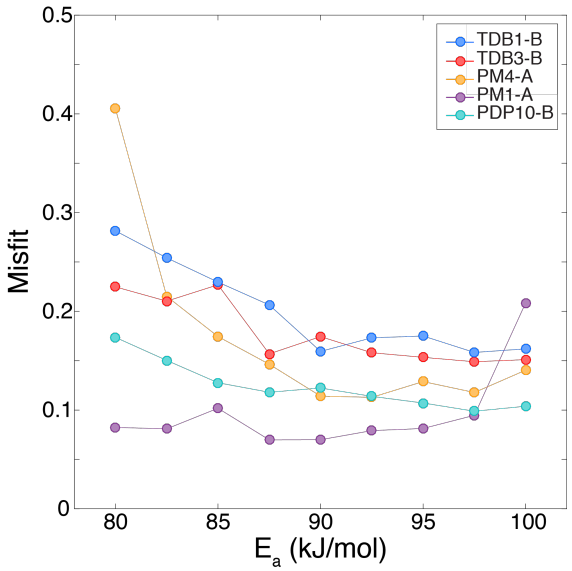

Figure 11: Minimized misfit between observed and MDD-modeled ^{3}He diffusivities as a function of activation energy E_a for Gesso Valley quartz samples, assuming a three-domain diffusion model. Pre-exponential factors and gas fractions for each domain covary with E_a; we show misfit as a function of E_a because it is assumed to be common to all diffusion domains in our modeling approach.

For example, the MDD misfit for the PM1-A step degassing experiment ranges between 7.0 and 10.2% between activation energies of 80 and 97.5 *kJ/mol* (Fig. 11). The MDD diffusion kinetics we use in the forward models for PM1 quartz presented above assume an activation energy of 89.6 *kJ/mol*. If instead we use a different set of diffusion kinetics for a three-domain model that

yields a comparable misfit with the step degassing experiment (E_a = 97.5 *kJ/mol*; $ln(D_0/a^2)$ = 12.2, 10.1, 16.8; f_{gas} = 0.45, 0.44, 0.11; Misfit = 0.095), we calculate an integrated EDT from the cosmogenic ^{3}He retention in PM1 quartz of 17.8 (± 2.3) +3.8/-3.9 ºC, which is in agreement with the integrated EDT we calculated for PM4 (Fig. 6). This highlights how sensitive the temperatures we calculate from an observed amount of cosmogenic ^{3}He retention are to the diffusion kinetics we use. While different MDD models might reproduce diffusivities observed in laboratory step degassing experiments comparably well, the downward extrapolation of these models results in significantly different diffusivities at the temperatures characterizing Earth's surface. This suggests that some or all of the intra-moraine differences in integrated EDTs could be attributed to uncertainties in how we extrapolate laboratory-determined diffusion kinetics. Given that we do not yet have a mechanistic understanding of what controls the complex noble gas diffusion behavior we observe in our experiments, discriminating between different MDD models of comparably good fit (and even assessing whether MDD models adequately represent the processes responsible for complex behavior) is difficult at this stage.

A third possible explanation for the intra-moraine variation could arise from our grain size analysis and scaling of MDD models. Uncertainty in the physical significance of our MDD models translates into an uncertainty in our assumptions about how to scale our MDD model fits from step degassing experiments to the cosmogenic ^{3}He measurements. However, because we have scaled the results of each experiment using the same assumptions in Eq. 1, the effects will be systematic. Similarly, the factor of 1.5 we applied to estimated spherical equivalent radii of quartz from the sieve fractions, based on different approaches to estimate surface area to volume ratios and ground truthing with x-ray computed tomography data, will have systematic effects on

all integrated EDTs. Assuming that the MDD model scaling and correction applied to sieve fraction measurements are appropriate, we must also consider the possibility that our grain size analysis for the PM and TDB samples does not represent the actual grain size and diffusion lengthscale of quartz in these samples. Since we did not have whole rock material from the original PM and TDB samples, we made thin sections from other boulders collected from the PM and TDB moraines to compare with the size distributions of quartz in the sieved fraction. While there is good agreement between the mean spherical equivalent radii of quartz measured in these thin sections and in the sieve fractions, it is possible that in the original sample the mean quartz size before crushing was much larger. As a sensitivity test, we again use PM1 as an example. In order to obtain an integrated EDT for PM1 equivalent to that calculated for PM4 of 19.7 ºC, we must increase the spherical equivalent radius assumed for the cosmogenic ^{3}He measurement by 110% (without changing the spherical equivalent radius for PM4). While such a dramatic underestimation of the PM1 grain size, and more generally >100% uncertainty in all our PM and TDB grain size analyses, seems unlikely, we cannot rule out such a possibility given that whole rock material from these samples was unavailable.

In summary, there is substantial intra-moraine variability in the integrated EDTs we calculate from our cosmogenic ^{3}He observations that requires explanation. Nonetheless, we calculate an integrated EDT for at least one sample from each moraine that is consistent with maximum seasonal temperatures in the TraCE-21ka simulation and from chironomid-based mean July temperature reconstructions. Given that we expect integrated EDTs to exceed the mean ambient temperatures in a sample's exposure history because of the nonlinear dependence of diffusivity on temperature, this agreement is promising for the application of cosmogenic noble gas

663 paleothermometry in paleoclimate studies. For the Maritime Alps specifically, this result may
664 indicate that this region experienced a Late Quaternary climatic history similar to the rest of the
665 western Alps, and that proximity to the Mediterranean Sea had a limited effect on the
666 temperatures of this region. Future application of cosmogenic noble gas paleothermometry to a
667 larger number of samples per moraine, as well as to more recently formed landforms whose
668 shading history can be better resolved, accompanied with further advances in our understanding
669 of noble gas diffusion kinetics, will allow for much improved reconstruction of
670 paleotemperatures in the future.
671
672 **5. Conclusions**
673 In summary, integrated EDTs since the LGM, calculated from our observations of cosmogenic
674 ^{3}He concentrations in quartz range from 8 to 25 ºC and are broadly consistent with what we
675 expect from modern meteorological station data, a GCM simulation of Earth's climate since the
676 LGM, and data from independent proxies in the region. Nonetheless, there are nontrivial
677 differences between the integrated EDTs we calculate, particularly for samples with equivalent
678 exposure ages from the same moraine, that require explanation. We identify three major potential
679 sources of uncertainty that could account for these discrepancies: (1) the fact that we have not
680 accounted for variations in radiative heating of the boulder surfaces across samples due to
681 differential shading, (2) limitations in our understanding of and ability to model and extrapolate
682 helium diffusion kinetics when complex behavior is observed, or (3) uncertainties associated
683 with our quartz grain size analyses. At this stage, all three of these possibilities could be
684 contributing to intra-moraine and inter-moraine variability in reconstructed temperatures.
685 Because of these nontrivial uncertainties, and the fact that we have no cosmogenic ^{3}He

observations from younger moraines that record only more recent, Holocene temperatures in the Gesso Valley, it is difficult to fully compare our results to the TraCE-21ka and chironomid temperature records and not yet possible to comment on the hypothesis that the post-LGM climate evolution and glacier dynamics of the Maritime Alps differed from other Alpine regions. Nonetheless these results are promising, and suggest that with additional work and better understanding of diffusion kinetics and rock-air temperature relationships we can address questions in paleoclimate like this one in future applications.

Acknowledgements

MMT and DLS acknowledge support from the NSF Petrology and Geochemistry Program (EAR-1322086), the UC Berkeley Larsen Grant, and the Ann and Gordon Getty Foundation. MMT was supported by an NSF Graduate Research Fellowship. MS acknowledges support from the Royal Society (IE150603), the Leverhulme Trust (IAF-2016-001) and NERC (CIAF 9092.1010).

References

Abràmoff, M.D., Magalhães, P.J., Ram, S.J., 2004. Image processing with ImageJ. Biophotonics international 11, 36–42.

Annan, J.D., Hargreaves, J.C., 2015. A perspective on model-data surface temperature comparison at the Last Glacial Maximum. Quat. Sci. Rev. 107, 1–10.

Annan, J.D., Hargreaves, J.C., 2013. A new global reconstruction of temperature changes at the Last Glacial Maximum. Clim. Past 9, 367–376.

Balco, G., Stone, J.O., Lifton, N.A., Dunai, T.J., 2008. A complete and easily accessible means

709 of calculating surface exposure ages or erosion rates from ^{10}Be and ^{26}Al measurements.
710 Quat. Geochronol. 3, 174–195.
711 Bartlein, P.J., Harrison, S.P., Brewer, S., Connor, S., Davis, B., Gajewski, K., Guiot, J.,
712 Harrison-Prentice, T.I., Henderson, A., Peyron, O., Others, 2011. Pollen-based continental
713 climate reconstructions at 6 and 21 ka: a global synthesis. Clim. Dyn. 37, 775–802.
714 Bartlett, M.G., Chapman, D.S., Harris, R.N., 2006. A decade of ground--air temperature tracking
715 at Emigrant Pass Observatory, Utah. J. Clim. 19, 3722–3731.
716 Brisset, E., Guiter, F., Miramont, C., Revel, M., Anthony, E.J., Delhon, C., Arnaud, F., Malet, E.,
717 de Beaulieu, J.-L., 2015. Lateglacial/Holocene environmental changes in the Mediterranean
718 Alps inferred from lacustrine sediments. Quat. Sci. Rev. 110, 49–71.
719 Buckenham, M.H., Rogers, J., 1954. Flotation of quartz and feldspar by dodecylamine.
720 Transactions of Institute of Mining and Metallurgy 64, l–30.
721 Casazza, G., Grassi, F., Zecca, G., Minuto, L., 2016. Phylogeographic Insights into a Peripheral
722 Refugium: The Importance of Cumulative Effect of Glaciation on the Genetic Structure of
723 Two Endemic Plants. PLoS One 11, e0166983.
724 Cheddadi, R., Bar-Hen, A., 2009. Spatial gradient of temperature and potential vegetation
725 feedback across Europe during the late Quaternary. Clim. Dyn. 32, 371–379.
726 Cheddadi, R., Yu, G., Guiot, J., Harrison, S.P., Prentice, I.C., 1996. The climate of Europe 6000
727 years ago. Clim. Dyn. 13, 1–9.
728 Collins, W.D., Bitz, C.M., Blackmon, M.L., Bonan, G.B., Bretherton, C.S., Carton, J.A., Chang,
729 P., Doney, S.C., Hack, J.J., Henderson, T.B., Others, 2006. The community climate system
730 model version 3 (CCSM3). J. Clim. 19, 2122–2143.
731 Davis, B.A.S., Brewer, S., Stevenson, A.C., Guiot, J., 2003. The temperature of Europe during

732 the Holocene reconstructed from pollen data. Quat. Sci. Rev. 22, 1701–1716.
733 Durand, Y., Giraud, G., Laternser, M., Etchevers, P., Mérindol, L., Lesaffre, B., 2009a.
734 Reanalysis of 47 years of climate in the French Alps (1958–2005): climatology and trends
735 for snow cover. J. Appl. Meteorol. Climatol. 48, 2487–2512.
736 Durand, Y., Laternser, M., Giraud, G., Etchevers, P., Lesaffre, B., Mérindol, L., 2009b.
737 Reanalysis of 44 yr of climate in the French Alps (1958–2002): methodology, model
738 validation, climatology, and trends for air temperature and precipitation. J. Appl. Meteorol.
739 Climatol. 48, 429–449.
740 Fechtig, H., Kalbitzer, S., 1966. The diffusion of argon in potassium-bearing solids, in:
741 Potassium Argon Dating. Springer, pp. 68–107.
742 Federici, P.R., Granger, D.E., Pappalardo, M., Ribolini, A., Spagnolo, M., Cyr, A.J., 2008.
743 Exposure age dating and Equilibrium Line Altitude reconstruction of an Egesen moraine in
744 the Maritime Alps, Italy. Boreas 37, 245–253.
745 Federici, P.R., Granger, D.E., Ribolini, A., Spagnolo, M., Pappalardo, M., Cyr, A.J., 2012. Last
746 Glacial Maximum and the Gschnitz stadial in the Maritime Alps according to ^{10}Be
747 cosmogenic dating. Boreas 41, 277–291.
748 Federici, P.R., Pappalardo, M., Ribolini, A., 2003. Geomorphological map of the Maritime Alps
749 Natural Park and surroundings (Argentera Massif, Italy). 1: 25,000 scale. Selca, Florence.
750 Federici, P.R., Ribolini, A., Spagnolo, M., 2017. Glacial history of the Maritime Alps from the
751 Last Glacial Maximum to the Little Ice Age. Geological Society, London, Special
752 Publications 433, 137–159.
753 Gandouin, E., Franquet, E., 2002. Late Glacial and Holocene chironomid assemblages in Lac
754 Long Inférieur (southern France, 2090 m): palaeoenvironmental and palaeoclimatic

implications. J. Paleolimnol. 28, 317–328.

Gardner, A.S., Sharp, M.J., Koerner, R.M., Labine, C., Boon, S., Marshall, S.J., Burgess, D.O., Lewis, D., 2009. Near-surface temperature lapse rates over Arctic glaciers and their implications for temperature downscaling. J. Clim. 22, 4281–4298.

Gourbet, L., Shuster, D.L., Balco, G., Cassata, W.S., Renne, P.R., Rood, D., 2012. Neon diffusion kinetics in olivine, pyroxene and feldspar: retentivity of cosmogenic and nucleogenic neon. Geochim. Cosmochim. Acta 86, 21–36.

Granger, D.E., Lifton, N.A., Willenbring, J.K., 2013. A cosmic trip: 25 years of cosmogenic nuclides in geology. Geol. Soc. Am. Bull. 125, 1379–1402.

Hall, K., Lindgren, B.S., Jackson, P., 2005. Rock albedo and monitoring of thermal conditions in respect of weathering: some expected and some unexpected results. Earth Surf. Processes Landforms 30, 801–812.

Harrison, S.P., Bartlein, P.J., Izumi, K., Li, G., Annan, J., Hargreaves, J., Braconnot, P., Kageyama, M., 2015. Evaluation of CMIP5 palaeo-simulations to improve climate projections. Nat. Clim. Chang. 5, nclimate2649.

Harrison, T.M., Lovera, O.M., Matthew, T.H., 1991. $^{40}Ar/^{39}Ar$ results for alkali feldspars containing diffusion domains with differing activation energy. Geochim. Cosmochim. Acta 55, 1435–1448.

He, F., 2011. Simulating transient climate evolution of the last deglaciation with CCSM 3.

Heilbronner, R., Barrett, S., 2013. Image analysis in Earth sciences: microstructures and textures of earth materials. Springer Science & Business Media.

Heiri, O., Brooks, S.J., Renssen, H., Bedford, A., Hazekamp, M., Ilyashuk, B., Jeffers, E.S., Lang, B., Kirilova, E., Kuiper, S., Others, 2014. Validation of climate model-inferred

778 regional temperature change for late-glacial Europe. Nat. Commun. 5, 4914.
779 Heiri, O., Millet, L., 2005. Reconstruction of Late Glacial summer temperatures from
780 chironomid assemblages in Lac Lautrey (Jura, France). J. Quat. Sci. 20, 33–44.
781 Heiri, O., Tinner, W., Lotter, A.F., 2004. Evidence for cooler European summers during periods
782 of changing meltwater flux to the North Atlantic. Proc. Natl. Acad. Sci. U. S. A. 101,
783 15285–15288.
784 Hughes, P.D., Woodward, J.C., 2017. Quaternary glaciation in the Mediterranean mountains: a
785 new synthesis. Geological Society, London, Special Publications 433, 1–23.
786 Ilyashuk, E.A., Koinig, K.A., Heiri, O., Ilyashuk, B.P., Psenner, R., 2011. Holocene temperature
787 variations at a high-altitude site in the Eastern Alps: a chironomid record from Schwarzsee
788 ob Sölden, Austria. Quat. Sci. Rev. 30, 176–191.
789 Ivy-Ochs, S., Kober, F., Alfimov, V., Kubik, P.W., Synal, H.-A., 2007. Cosmogenic ^{10}Be, ^{21}Ne
790 and ^{36}Cl in sanidine and quartz from Chilean ignimbrites. Nucl. Instrum. Methods Phys.
791 Res. B 259, 588–594.
792 Jost, A., Lunt, D., Kageyama, M., Abe-Ouchi, A., Peyron, O., Valdes, P.J., Ramstein, G., 2005.
793 High-resolution simulations of the last glacial maximum climate over Europe: a solution to
794 discrepancies with continental palaeoclimatic reconstructions? Clim. Dyn. 24, 577–590.
795 Kessler, M.A., Anderson, R.S., Stock, G.M., 2006. Modeling topographic and climatic control of
796 east-west asymmetry in Sierra Nevada glacier length during the Last Glacial Maximum.
797 Journal of Geophysical Research: Earth Surface 111.
798 Ketcham, R.A., 2005. Computational methods for quantitative analysis of three-dimensional
799 features in geological specimens. Geosphere 1, 32–41.
800 Kuhlemann, J., Rohling, E.J., Krumrei, I., Kubik, P., Ivy-Ochs, S., Kucera, M., 2008. Regional

synthesis of Mediterranean atmospheric circulation during the Last Glacial Maximum. Science 321, 1338–1340.

Larocque, I., Finsinger, W., 2008. Late-glacial chironomid-based temperature reconstructions for Lago Piccolo di Avigliana in the southwestern Alps (Italy). Palaeogeogr. Palaeoclimatol. Palaeoecol. 257, 207–223.

Liu, Z., Otto-Bliesner, B.L., He, F., Brady, E.C., Tomas, R., Clark, P.U., Carlson, A.E., Lynch-Stieglitz, J., Curry, W., Brook, E., Others, 2009. Transient simulation of last deglaciation with a new mechanism for Bølling-Allerød warming. Science 325, 310–314.

Loomis, S.E., Russell, J.M., Verschuren, D., Morrill, C., De Cort, G., Damsté, J.S.S., Olago, D., Eggermont, H., Street-Perrott, F.A., Kelly, M.A., 2017. The tropical lapse rate steepened during the Last Glacial Maximum. Science advances 3, e1600815.

Lovera, O.M., Grove, M., Mark Harrison, T., Mahon, K.I., 1997/8. Systematic analysis of K-feldspar $^{40}Ar/^{39}Ar$ step heating results: I. Significance of activation energy determinations. Geochim. Cosmochim. Acta 61, 3171–3192.

Lovera, O.M., Richter, F.M., 1989. The $^{40}Ar/^{39}Ar$ Thermochronometry for Slowly Cooled Samples. J. Geophys. Res. 94, 17–917.

Lovera, O.M., Richter, F.M., Harrison, T.M., 1991. Diffusion domains determined by ^{39}Ar released during step heating. J. Geophys. Res. 96, 2057–2069.

Masson-Delmotte, V., Schulz, M., Abe-Ouchi, A., Beer, J., Ganopolski, A., González Rouco, J.F., Jansen, E., Lambeck, K., Luterbacher, J., Naish, T., Osborn, T., Otto-Bliesner, B., Quinn, T., Ramesh, R., Rojas, M., Shao, X., Timmermann, A., 2013. Information from paleoclimate archives, in: Stocker, T.F., Qin, D., Plattner, G.-K., Tignor, M., Allen, S.K., Boschung, J., Nauels, A., Xia, Y., Bex, V., Midgley, P.M. (Eds.), Climate Change 2013:

824 The Physical Science Basis. Contribution of Working Group I to the Fifth Assessment
825 Report of the Intergovernmental Panel on Climate Change. Cambridge University Press,
826 Cambridge, United Kingdom, and New York, NY, USA, pp. 383–464.
827 McGreevy, J.P., 1985. Thermal properties as controls on rock surface temperature maxima, and
828 possible implications for rock weathering. Earth Surf. Processes Landforms 10, 125–136.
829 Nishiizumi, K., Imamura, M., Caffee, M.W., Southon, J.R., Finkel, R.C., McAninch, J., 2007.
830 Absolute calibration of ^{10}Be AMS standards. Nucl. Instrum. Methods Phys. Res. B 258,
831 403–413.
832 Schmidt, G.A., Annan, J.D., Bartlein, P.J., Cook, B.I., Guilyardi, E., Hargreaves, J.C., Harrison,
833 S.P., Kageyama, M., LeGrande, A.N., Konecky, B., Lovejoy, S., Mann, M.E., Masson-
834 Delmotte, V., Risi, C., Thompson, D., Timmermann, A., Tremblay, L.-B., Yiou, P., 2014.
835 Using palaeo-climate comparisons to constrain future projections in CMIP5. Clim. Past 10,
836 221–250.
837 Schmittner, A., Urban, N.M., Shakun, J.D., Mahowald, N.M., Clark, P.U., Bartlein, P.J., Mix,
838 A.C., Rosell-Melé, A., 2011. Climate sensitivity estimated from temperature reconstructions
839 of the Last Glacial Maximum. Science 334, 1385–1388.
840 Schwarz, N., Schlink, U., Franck, U., Großmann, K., 2012. Relationship of land surface and air
841 temperatures and its implications for quantifying urban heat island indicators--An
842 application for the city of Leipzig (Germany). Ecol. Indic. 18, 693–704.
843 Shuster, D.L., Cassata, W.S., 2015. Paleotemperatures at the lunar surfaces from open system
844 behavior of cosmogenic ^{38}Ar and radiogenic ^{40}Ar. Geochim. Cosmochim. Acta 155, 154–
845 171.
846 Shuster, D.L., Farley, K.A., 2005. Diffusion kinetics of proton-induced ^{21}Ne, ^{3}He, and ^{4}He in

847 quartz. Geochim. Cosmochim. Acta 69, 2349–2359.
848 Shuster, D.L., Farley, K.A., Sisterson, J.M., Burnett, D.S., 2004. Quantifying the diffusion
849 kinetics and spatial distributions of radiogenic ^{4}He in minerals containing proton-induced
850 ^{3}He. Earth Planet. Sci. Lett. 217, 19–32.
851 Stone, J.O., 2000. Air pressure and cosmogenic isotope production. J. Geophys. Res. [Solid
852 Earth] 105, 23753–23759.
853 Tremblay, M.M., Shuster, D.L., Balco, G., 2014a. Cosmogenic noble gas paleothermometry.
854 Earth Planet. Sci. Lett. 400, 195–205.
855 Tremblay, M.M., Shuster, D.L., Balco, G., 2014b. Diffusion kinetics of ^{3}He and ^{21}Ne in quartz
856 and implications for cosmogenic noble gas paleothermometry. Geochim. Cosmochim. Acta
857 142, 186–204.
858 Tremblay, M.M., Shuster, D.L., Balco, G., Cassata, W.S., 2017. Neon diffusion kinetics and
859 implications for cosmogenic neon paleothermometry in feldspars. Geochim. Cosmochim.
860 Acta 205, 14–30.
861 Vermeesch, P., Baur, H., Heber, V.S., Kober, F., Oberholzer, P., Schaefer, J.M., Schlüchter, C.,
862 Strasky, S., Wieler, R., 2009. Cosmogenic ^{3}He and ^{21}Ne measured in quartz targets after one
863 year of exposure in the Swiss Alps. Earth Planet. Sci. Lett. 284, 417–425.
864 von der Heydt, A.S., Dijkstra, H.A., van de Wal, R.S.W., Caballero, R., Crucifix, M., Foster,
865 G.L., Huber, M., Köhler, P., Rohling, E., Valdes, P.J., Ashwin, P., Bathiany, S., Berends, T.,
866 van Bree, L.G.J., Ditlevsen, P., Ghil, M., Haywood, A.M., Katzav, J., Lohmann, G.,
867 Lohmann, J., Lucarini, V., Marzocchi, A., Pälike, H., Baroni, I.R., Simon, D., Sluijs, A.,
868 Stap, L.B., Tantet, A., Viebahn, J., Ziegler, M., 2016. Lessons on Climate Sensitivity From
869 Past Climate Changes. Curr Clim Change Rep 2, 148–158.

870 Wu, H., Guiot, J., Brewer, S., Guo, Z., 2007. Climatic changes in Eurasia and Africa at the last
871 glacial maximum and mid-Holocene: reconstruction from pollen data using inverse
872 vegetation modelling. Clim. Dyn. 29, 211–229.